PCCP

PAPER

View Article Online
View Journal | View Issue





Cite this: *Phys. Chem. Chem. Phys.*, 2017, **19**, 13140

# Observation of crystalline changes of titanium dioxide during lithium insertion by visible spectrum analysis†

Inho Nam,‡[a] Jongseok Park,‡[a] Soomin Park,[a] Seongjun Bae,[a] Young Geun Yoo,[a] Jeong Woo Han[b] and Jongheop Yi*[a]

Received 14th March 2017,
Accepted 24th April 2017

DOI: 10.1039/c7cp01613a

rsc.li/pccp

Real-time analysis of changes in the atomic environment of materials is a cutting edge technology that is being used to explain reaction dynamics in many fields of science. Previously, this kind of analysis was only possible using heavy nucleonic equipment such as XANES and EXAFS, or Raman spectroscopy on a moderate scale. Here, a new methodology is described that can be used to track changes in crystalline developments during complex Li insertion reactions *via* the observation of structural color. To be specific, the changes in atomic crystalline and nanostructure are shown during Li insertion in a complex $TiO_2$ polymorph. Structural color corresponds to the refractive indices of materials originating from their atomic bonding nature and precise wave interferences in accordance with their nanostructure. Therefore, this new analysis simultaneously reveals changes in the nanostructure as well as changes in the atomic bonding nature of materials.

## Introduction

Butterflies have beautiful and complex colors that originate from the submicron patterned structures in their wings.[1,2] Analogously, it is widely regarded that the nanostructure, such as in photonic crystals, creates the color,[3,4] which is one of the fundamental optical properties of materials. Structural color corresponds to parameters such as precise wave interferences by the nanostructure and differences between the refractive indices of crystalline materials and their environment. Wave interference is mainly related to the microscopic structure, which means that we can tune the wave interference *via* precise nanostructuring.[3,5] On the other hand, the refractive index is a fundamental property of materials, and is closely related to the electronic polarizability of ions in crytal and to local fields inside the material, which means that there exists a correlation between the structural colors and the nature of the atomic bonding of materials.[6] As a consequence, this correlation indicates that we can possibly analyze a change in (i) the atomic crystalline and (ii) the nanostructure in materials by observing vivid colors and their visible reflectance spectra *via* time-on-stream.

Here, we show a new method for analyzing changes in the atomic crystallinity of an energy material during complex Li insertion reactions simply *via* the observation of the color and visible spectra of the material. This method is particularly powerful in its description of the overall kinetics; to be specific, electrochemical energy storage systems ($Li^+$ or $Na^+$ batteries) comprise one of the best conceptual examples, because tracking crystalline changes during sequential reactions is critically needed in this field,[7,8] and this includes observing the tolerance related to the nanostructure collapse.[9,10] As a practical example for the proof of this concept, we observed the Li insertion reaction in complex $TiO_2$ polymorphs ($TiO_2 + xLi \rightarrow Li_xTiO_2$) *via* changes in their structural color and detailed reflectance spectra. This reaction is a good example of our method because the electrochemical characteristics of $TiO_2$ highly depend on their structural parameters such as crystallinity and polymorphs.[11–14] This phenomenon is well interpreted by general *ab initio* principles and Maxwell's equations without any empirical limiting factors; therefore, we expect that our method can be applied to general types of materials and reactions.

## Experimental section

### Fabrication of complex $TiO_2$ polymorph with hexagonal nanostructuring

Complex $TiO_2$ polymorphs were chemically deposited onto a Ti foil *via* direct two-step electrochemical anodization using

[a] *School of Chemical and Biological Engineering, WCU Program of $C_2E_2$, ICP, Seoul National University, Seoul 08826, Republic of Korea. E-mail: jyi@snu.ac.kr*
[b] *Department of Chemical Engineering, University of Seoul, Seoul 02504, Republic of Korea*

† Electronic supplementary information (ESI) available: Supplementary Fig. S1–S10. See DOI: 10.1039/c7cp01613a

‡ These authors contributed equally to this work.

 

methods described in our previous research.[15] A two-electrode cell, using Ti foil (Sigma-Aldrich) as a working electrode and a Pt mesh as a counter electrode, was utilized. The back of the Ti foil was protected by an electrically inactive tape to allow it to function as a current collector. Anodization was conducted in an electrolyte containing 3% (wt/vol) $NH_4F$ and 3% (vol) $H_2O$ in ethylene glycol (Samchun Chemicals).[16] The anodization was divided by a two-step process, which included a peeling-off process. The first anodization was conducted for 1.5 hours to form hexagonally arranged $TiO_2$ nanotubes under a constant voltage of 30 V. Immediate sonication in deionized water loosened the attachment between $TiO_2$ and the Ti surface to allow the $TiO_2$ layer to be simply peeled off using a commercial sticky tape. The second anodization was conducted under the same conditions as the first with the exception of the duration (1 minute), and the subsequent calcination of the substrate. The as-fabricated structure had a mixed phase that included anatase and rutile (48 : 52) and showed vivid color (Fig. 1).

## Characterization

In order to prove this concept, the as-fabricated $TiO_2$ film was used as an electrode that was pre-operated for 20 discharge–charge cycles. Li metal was used as a counter electrode and an electrolyte was prepared by adding 1.15 M $LiPF_6$ to a mixture of ethylene carbonate, ethyl methyl carbonate, and diethyl carbonate (EC : EMC : DEC = 3 : 5 : 2). During a discharge reaction immediately after the pre-operation cycles, we analyzed the differences in the colors of the electrode in three states of charge (0, 0.25 and 0.5 of $x$ in $Li_xTiO_2$) using a charge-coupled device (CCD) camera and reflectance spectra. The reflectance spectra were obtained *via* ultraviolet-visible diffuse reflectance spectroscopy (UV-Vis-DRS, V670, Jasco) and the model reaction, $TiO_2 + 0.5\ Li \rightarrow Li_{0.5}TiO_2$, was conducted under galvanostatic discharge–charge conditions (WonATech WBCS3000). The current density was 5 μA $cm^{-2}$, which was low enough to closely determine the ideal Li insertion reaction in $TiO_2$. The scanning electron microscopy (SEM) images of the $TiO_2$ nanostructure were obtained using a field-emission SEM operated at 2 kV with an in-lens detector (Sigma, Carl Zeiss). An X-ray diffractometer (XRD, Rigaku, D/max-2200) was utilized to investigate the crystalline nature of the samples. For the analyses, the electrodes were washed with a diethylene carbonate solvent to eliminate all residual electrolytes.

## *Ab initio* calculations

*Ab initio* calculations were carried out on the basis of periodic density functional theory (DFT) using a generalized gradient approximation (GGA) within the Perdew–Burke–Ernzerhof (PBE) exchange correction functional.[17,18] We used the projector augmented wave (PAW) method to describe ionic cores as implemented in the Vienna ab initio simulation package (VASP).[19] DFT+$U$ within Dudarev's approach was also used with $U_{eff}$ = 4.2 to account for the onsite Coulomb interactions in the localized d orbital of Ti.[20–22] The wave functions were constructed from the expansion of plane waves with an energy cutoff of 520 eV. For anatase $TiO_2$ and orthorhombic $Li_{0.5}TiO_2$, a 3 × 5 × 2 $k$-point mesh was used as described in the Monkhorst–Pack method, and for rutile $TiO_2$ and monoclinic $Li_{0.5}TiO_2$, a 4 × 3 × 4 $k$-point mesh was used to sample the Brillouin zone. The electronic optimization steps were converged self-consistently over $10^{-5}$ eV per formula unit. The supercell of anatase $TiO_2$ was composed of 8 Ti and 16 O atoms ($Ti_8O_{16}$), rutile $TiO_2$ was composed of 4 Ti and 8 O atoms ($Ti_4O_8$), orthorhombic $Li_{0.5}TiO_2$ was composed of 4 Li, 8 Ti and 16 O atoms ($Li_4Ti_8O_{16}$), and monoclinic $Li_{0.5}TiO_2$ was composed of 2 Li, 4 Ti and 8 O atoms ($Li_2Ti_4O_8$).

A Li insertion voltage *versus* the composition plot shown in Fig. 2(a) was calculated as follows:[23]

$$V = -\frac{G[Li_{0.5}TiO_2] - G[TiO_2] - 0.5G[Li]}{0.5} \quad (1)$$

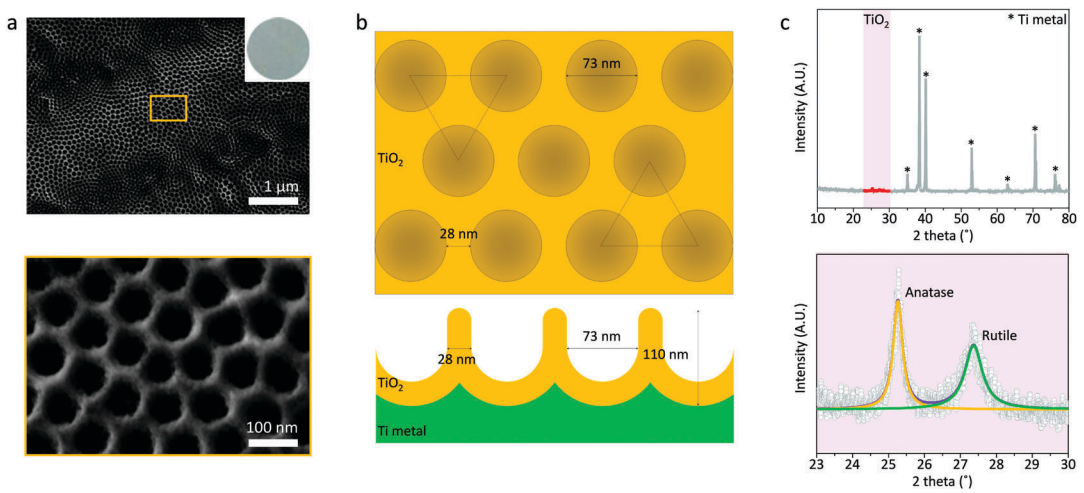


Fig. 1 Characteristic features of the $TiO_2$ polymorph deposited on the Ti metal foil. (a) SEM image of an as-prepared mixed-phase $TiO_2$ polymorph. Inset is a photograph of the corresponding $TiO_2$ sample. (b) Schematic illustrations of a hexagonal arrangement of pores in as-prepared $TiO_2$ film on the titanium substrate. (c) XRD patterns of the $TiO_2$ polymorph anodically grown on titanium foil. The areas under the anatase (101) and rutile (110) peaks indicate the ratio in which anatase and rutile phase $TiO_2$ are mixed in the material.

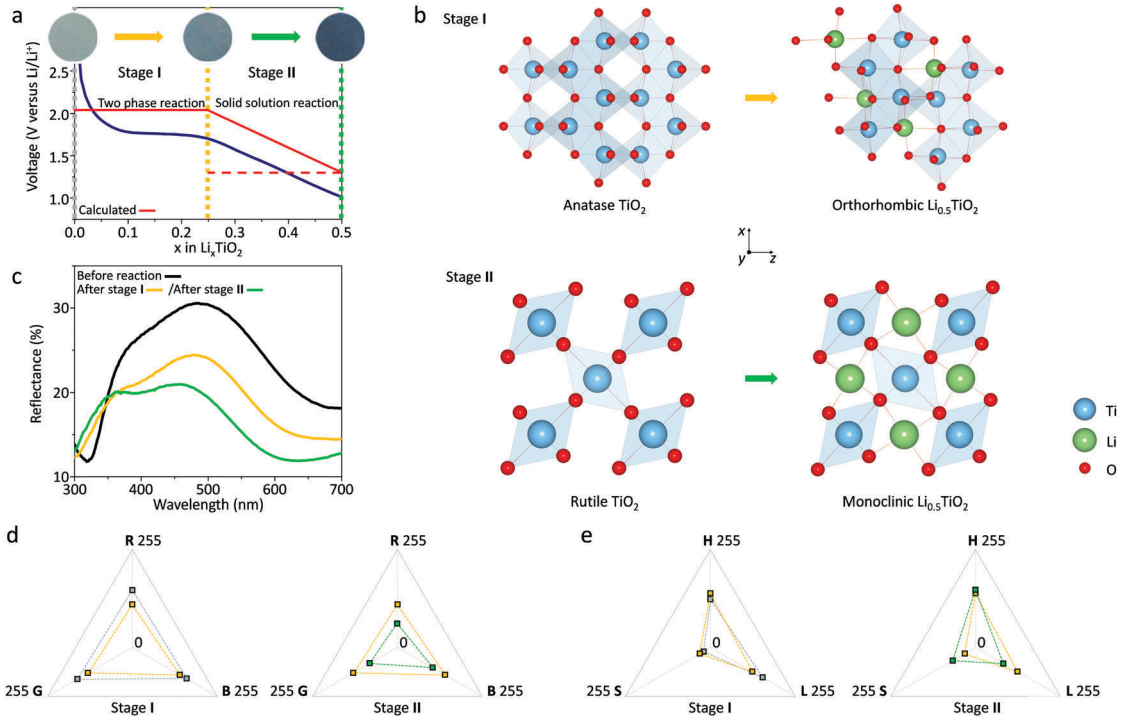


Fig. 2 Change in crystalline induced by the Li insertion reaction from $TiO_2$ to $Li_{0.5}TiO_2$. (a) Electrochemical potential profiles of a mixed-phase $TiO_2$ polymorph based on experimental (blue line) and calculated (red line) values during the lithium insertion process. (b) Description of each distortion in the crystalline of anatase and rutile $TiO_2$ after lithium insertion. (c) Reflectance spectra of the as-prepared $TiO_2$ polymorph (black line), after stages I (yellow line) and II (green line), respectively. (d and e) Detailed optical analysis (red(**R**)|green(**G**)|blue(**B**) and hue(**H**)|saturation(**S**)|luminance(**L**)) of $TiO_2$ polymorphs in each lithium insertion state.

where $G$ is the Gibbs free energy of the compound. $Li_{0.5}TiO_2$ is an orthorhombic or monoclinic phase and $TiO_2$ is the anatase or rutile phase, respectively. Here, $\Delta G \equiv \Delta E + P\Delta V - T\Delta S$. In this equation, the volume effects and entropic effects are neglected due to the low order of $P\Delta V$ (10–5 eV) and to the relatively small value of $T\Delta S$ compared to $\Delta E$. Therefore, the thermodynamic Li insertion voltage was calculated using the DFT total energy of the compounds.

### Calculations of dielectric function

The 3 × 3 Cartesian tensor for the complex imaginary dielectric function, $\varepsilon^{(2)}_{\alpha\beta}(\omega)$, was derived *via* the projector augmented wave (PAW) methodology.[24]

$$\varepsilon^{(2)}_{\alpha\beta}(\omega) = \frac{4\pi^2 e^2}{\Omega}\lim_{q\to 0}\frac{1}{q^2}\sum_{c,v,\mathbf{k}} 2w_{\mathbf{k}}\delta(\varepsilon_{c\mathbf{k}} - \varepsilon_{v\mathbf{k}} - \omega) \times \left\langle u_{c\mathbf{k}+\mathbf{e}_\alpha q} \middle| u_{v\mathbf{k}} \right\rangle \left\langle u_{c\mathbf{k}+\mathbf{e}_\beta q} \middle| u_{v\mathbf{k}} \right\rangle^* \quad (2)$$

where $\Omega$ is the volume of the primitive cell, $q$ is the scalar value of the Bloch vector of an incident wave at various wavelengths, $\omega$ and $w_k$ make up the $k$-point weight, and the vectors $\mathbf{e}_{\alpha,\beta}$ are the unit vectors for the three Cartesian directions. The indices $c$ and $v$ are restricted to the conduction and the valence band states, respectively. The real part of the dielectric function derives from the Kramers–Kronig relationship, as follows:

$$\varepsilon^{(1)}_{\alpha\beta}(\omega) = 1 + \frac{2}{\pi}P\int_0^\infty \frac{\varepsilon^{(2)}_{\alpha\beta}(\omega')\omega'}{\omega'^2 - \omega^2}\mathrm{d}\omega' \quad (3)$$

where $P$ denotes the principal value.[24] From the average values of calculated dielectric functions, the real $n(\omega)$ and imaginary $k(\omega)$ parts of the refractive index are given by the following:[25]

$$n(\omega) = \left[\frac{\sqrt{\varepsilon^{(1)}(\omega)^2 + \varepsilon^{(2)}(\omega)^2} + \varepsilon^{(1)}(\omega)}{2}\right]^{1/2} \quad (4)$$

$$k(\omega) = \left[\frac{\sqrt{\varepsilon^{(1)}(\omega)^2 + \varepsilon^{(2)}(\omega)^2} - \varepsilon^{(1)}(\omega)}{2}\right]^{1/2} \quad (5)$$

### 3-D FDTD simulations

Precise calculations to show the fingerprinted reflectance of materials in the visible wavelength region were conducted *via* a combined computational simulation between DFT+$U$ calculations to obtain the dielectric functions of materials, and a 3-D FDTD simulation used to solve Maxwell's equations related to the nanostructure. The 3-D FDTD calculation was performed using the OptiFDTD package, which is a numerical computer-aided drafting (CAD) environment based on the discrete Curl–Maxwell equations by iteration over time.[26] To obtain a reasonable field-enhancement resolution, the delta meshes were set to 4, 4 and 5 nm in the direction of $x$, $y$ and $z$, respectively. The simulation time step size was $7 \times 10^{-18}$ and the number of time steps was 741. To calculate the reflectance of materials, the electric field distribution was simulated to match the surroundings of

 

the precise nanostructure (the atmosphere refers to air). Plane wave light with polarization along the right-hand circle was considered in our model, and the light passed along the *z*-axis. To simulate a periodic layout using the plane wave, the boundaries of the *x*- and *y*-axis were set up as periodic boundary conditions. The input amplitude of light was 1.0 V $m^{-2}$. The real and imaginary parts of the refractive indices were calculated by dielectric functions from the above DFT calculations at various wavelengths in the visible region. Using the calculation, we obtained the $\mathbf{E}_x$ and $\mathbf{E}_y$ of electric components, which were the same as those in the hexagonal bowl-like nanostructure. On the other hand, these values were definitely different in the slit structure. The calculated reflectance spectra were derived by the average scalar values of the reflective $E_s$ in the *x*- and *y*-directions.

## Results and discussion

The scheme for the method is as follows: (1) a material to be analyzed is located on the periodic nano-bumpy substrate (inducement of wave interference) during the Li insertion reaction; and, (2) changes in color are observed using a charge-coupled device (CCD) camera (observation of the refractive index) and visible spectrometry (Fig. S1, ESI†). Here, we used a simple anodization method established in our previous research (see the Experimental section), to fabricate a complex $TiO_2$ polymorph-deposited surface with a precisely arranged nanostructure.[15] The $TiO_2$ deposited surface had uniform nanoscale hexagonal pores (the structure detail is shown in Fig. 1(a) and (b)) that induced a distinguishable wave interference and a structural color (inset of Fig. 1(a)). X-ray diffraction (XRD) analysis of the material on the surface before the reaction showed crystalline $TiO_2$ with mixed anatase and rutile phases (Fig. 1(c)). The ratio of anatase and rutile was 48 : 52, as derived using the Spurr and Myers's equation:[27,28]

$$[A]/\% = \frac{100 \times I_A}{I_A + 1.265 \times I_R} \quad (6)$$

where $[A]$ is the anatase content, and $I_A$ and $I_R$ correspond to the areas of the anatase (101) and rutile (110) XRD peaks, respectively. Various nanostructured inorganic materials developed in many previous studies, such as $SiO_2$, GaAs, $In_2O_3$, and $Al_2O_3$, could be fabricated as a photonic crystalline.

During a galvanostatic Li insertion reaction, a change in the color was observed *via* a CCD camera system corresponding to voltage *versus* composition data and the reaction steps, as shown in Fig. 2(a) and (b). The inherent reflectance curves of the materials in the visible wavelength region appeared as shown in Fig. 2(c). The red (**R**), green (**G**), blue (**B**), hue (**H**), saturation (**S**) and luminance (**L**) values were also obtained using the additive RGB and HSL model for the corresponding CCD images of the material surfaces (Fig. 2(d) and (e)). As reported, the reaction steps of the Li insertion were as follows:[12–14] first, there was a phase separation of $Li_xTiO_2$ into tetragonal ($TiO_2$, anatase) and orthorhombic ($Li_{0.5}TiO_2$) phases, which could be referred to as an early two-phase region in the voltage profile (voltage $>1.55$ V, referred to as Stage I in Fig. 2(b)).[12,14] Subsequently, rutile crystalline was converted from its initial tetragonal symmetry ($TiO_2$, rutile) toward a new phase that was indexed with a monoclinic space group ($P2/m$, $Li_{0.5}TiO_2$).[13] This reaction has an extended solid solution domain up to an insertion fraction of $x = 0.5$ (referred to as Stage II in Fig. 2(b)). When anatase $TiO_2$ changed to orthorhombic $Li_{0.5}TiO_2$ (stage I), its reflectance was diminished in the overall range of measurement because of a decrease in the energy bandgap of the material. In stage II (rutile changes to monoclinic $Li_{0.5}TiO_2$), a distinctive large curve shoulder of the reflectance spectra was observed in a short wavelength region ($<400$ nm), which was more apparent in the additive RGB mode (Fig. 2(d)). In stages I and II, the value of **B** was rarely decreased compared with other values. On the other hand, the decrease in the **G** value was accelerated in stage II, which means that the **B** value was distinguished after stage II compared with that in stage I. The HSL mode shows other differences between the two stages. In stages I and II, the **H** values were gradually increased, which means that the color was blue shifted during the reaction steps. On the other hand, the **S** and **L** values in stage II rapidly changed compared with stage I (**S** was positively and **L** was negatively changed), which means that the color of the material after stage II had a greater contrast compared with the color of the material after stage I. During the sequential reaction, the atomic structure was not described using conventional XRD analyses (Fig. S2, ESI†), because the grains of the materials were reduced to sub-nanometer size, and the intensity of their peaks was decreased during the reversible reaction.[29–32]

The visible reflectance spectra showing inherent structural colors can represent the specific crystalline on a specific nanostructure. The theoretical correlation of the crystalline and its fingerprinted reflectance spectra can be described by calculations compiling *ab initio* principles and Maxwell's equations, on which we based our prediction that the specific band structures of materials have strong influences on the fingerprinted reflectance spectra of one another. As a representative band structure, the change in energy bandgap can be one of the main factors of a change in color. First of all, we calculated the differences in the theoretical band structures of materials *via* density functional theory using *U*-value (DFT+*U*) calculations (see the details in Experimental section and Fig. S3 in ESI†). The calculated bandgaps tend to underestimate experimental values, however, the tendency is reasonable.[20,33,34] The Li insertion voltage *versus* composition plot was calculated using the same method (Red line in Fig. 2(a)), which proved that the calculated values well reflected the tendency of the experimental states. The energy bandgap of orthorhombic $Li_{0.5}TiO_2$ was dramatically decreased from the value of anatase $TiO_2$, because the Ti $d_{xz}$ orbital took an additional electron from the Li atom during the Li insertion reaction (Fig. S3(b) in ESI†).[14] The difference between the band-gaps of rutile and monoclinic $Li_{0.5}TiO_2$ was also similar to that of anatase $TiO_2$ (Fig. S3(c) and (d) in ESI†). Therefore, the decrease in the bandgaps of anatase and rutile in the phase transition to orthorhombic and monoclinic $Li_{0.5}TiO_2$, respectively, showed a similar tendency toward decreasing reflectance in a high wavelength region in

stages I and II. However, the new valance band of monoclinic $Li_{0.5}TiO_2$ was related to the $d_{z^2}$ and $d_{x^2}$ orbitals in Ti, rather than to the Ti $d_{xz}$ orbital, and the reflectance fingerprints between orthorhombic and monoclinic $Li_{0.5}TiO_2$ were markedly different.

At the quantum mechanical level, the complex dielectric function was closely connected to the band structure. The calculated dielectric functions and refractive indices of materials using the band structure calculations are shown in Fig. S4 (ESI†). The 3-D FDTD calculation was performed based on the calculated refractive indices and discrete Curl–Maxwell equations by iteration over time (the calculation details are in the Experimental section).[26] To derive the theoretical reflectance spectra of the materials, an electric field distribution was numerically simulated for the surrounding of the nanostructure at various levels of $\omega$ for the incident wave in air atmosphere (Fig. 3(a) and Fig. S5–S7 in ESI†). Here, the distribution of reflected amplitudes of the electric field along the *x*-axis and the *y*-axis ($\mathbf{E}_x$ and $\mathbf{E}_y$) were exactly the same, because hexagonally located nanopores have a two-dimensional periodicity.

According to the above simulation method, the fingerprinted reflectance spectra of anatase and rutile $TiO_2$ and orthorhombic and monoclinic $Li_{0.5}TiO_2$ materials were described, as shown in Fig. 3(b). Before the reaction steps, the surface of the nanostructure included both anatase and rutile $TiO_2$. Therefore, by combining the fingerprinted reflectance spectra of anatase and rutile $TiO_2$, we could represent the calculated reflectance curve before the Li insertion reaction. Accordingly, by combining the reflectance spectra of rutile $TiO_2$ and orthorhombic $Li_{0.5}TiO_2$, we could describe the reflectance curve after stage I. Finally, by combining the values of orthorhombic and monoclinic $Li_{0.5}TiO_2$, the reflectance curve after stage II was represented (Fig. 3(c)). Before stage I, a significant peak in the middle range of the wavelength (green) occurred in both the experimental and calculated values. After stage I, the significant peak was decreased, and after stage II, a shoulder peak in the reflectance curve occurred at 400 nm of the wavelength. The theoretical shoulder was relatively larger than the experimental values. The main reason for the difference between experiments and theoretic expectations is the inherent error of DFT-DOS simulations, which exists to date.[20,33,34] However, as shown by the experimental results, the decreasing tendency of the green light and increasing tendency of the blue light as a shoulder peak each could be easily explained using the calculating approach. In conclusion, the phenomena whereby color represents the atomic structure can be understood using an *ab initio* principle without any specific factors, and it can be interpreted by a deconvolution of the reflectance curve shapes, which means that this method is broadly applicable to an understanding of general chemical reactions.

It is reasonable to assume that a change in the nanostructure can also be detected *via* a change in reflectance spectra, which is because the reflectance spectra are related not only to the refractive index but also to the structural inducement of wave interference.[3–5] Although $TiO_2$ is a very stable material for applications to electrochemical energy storage *via* reversible Li insertion/desertion reactions, charging degradation sometimes occurs in a mixed-phase $TiO_2$ polymorph surface. For uncertain reasons, this phenomenon is caused by a progressive degradation of the initial precise nanostructure.[35–37] Cyclic charging retention analysis of a structure with occasional charge degradation is shown in Fig. S8 (ESI†), and a comparison with general

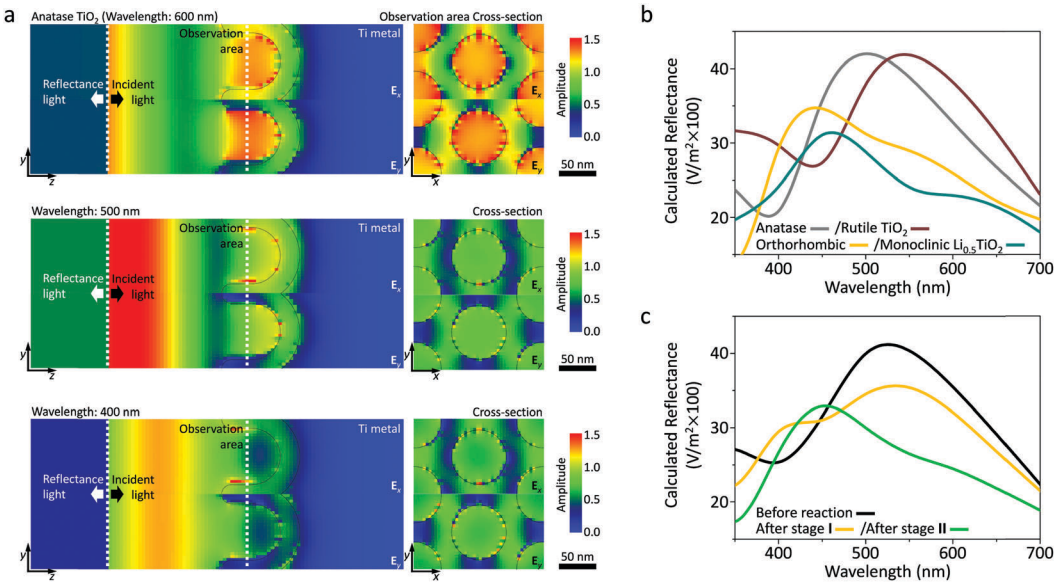


Fig. 3 3D-FDTD simulation of electromagnetic wave propagations by the surface of anatase $TiO_2$ in the hexagonal pore structure and reflectance spectra of various titania samples. (a) Simulated electric fields in each plane axis ($\mathbf{E}_x$, $\mathbf{E}_y$) at specific wavelengths (from the top to the bottom, 600, 500 and 400 nm, respectively). 2D-plane wave incident light is reflected by the periodic structure of the anatase $TiO_2$ film. (b) Calculated reflectance spectra of anatase $TiO_2$ (grey), rutile $TiO_2$ (brown), orthorhombic $Li_{0.5}TiO_2$ (yellow), and monoclinic $Li_{0.5}TiO_2$ (green). (c) Calculated reflectance spectra of mixed-phase $TiO_2$. To obtain the reflectance spectrum (black) of the mixed-phase $TiO_2$ before the lithium insertion reaction, the mass ratio-weighted (from XRD results) sum of each reflectance spectrum (anatase, rutile) was obtained.

 

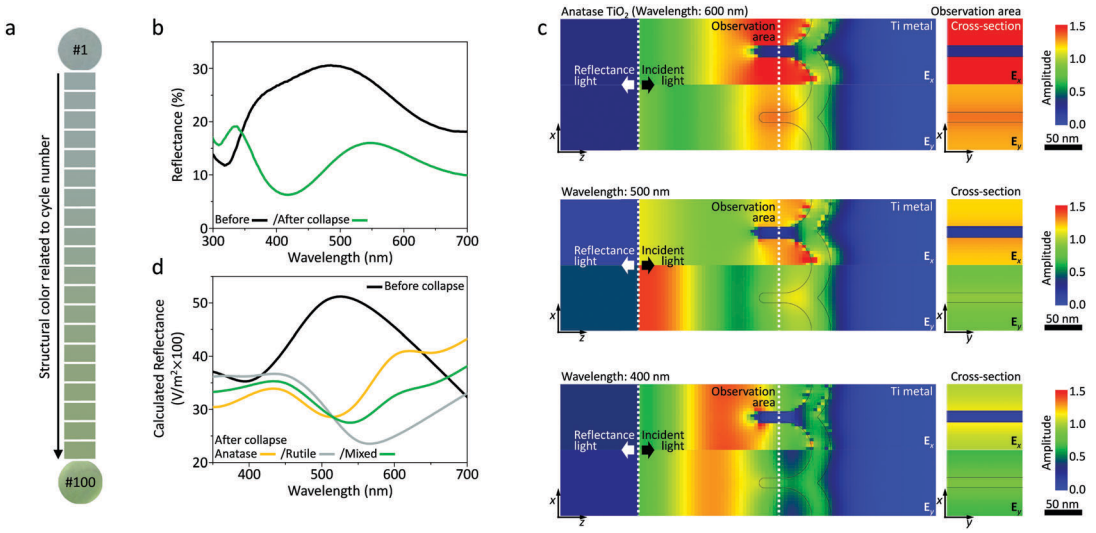


Fig. 4 Occasional degradation of the initial hexagonal structure upon cycling of lithium insertion. (a) Variation in the color of the $TiO_2$ polymorph during 100 cycles of lithium insertion/extraction. (b) The reflectance spectra of mixed-$TiO_2$ polymorph before (black) and after (green) the structural collapse induced by 100 cycles of lithiation. (c) Calculated distribution of the electric fields formed by the interference by the anatase $TiO_2$ film after structural collapse at various wavelengths. (d) Calculated reflectance of mixed-phase $TiO_2$ before structural collapse (black), anatase (yellow), rutile (grey) and mixed-phase $TiO_2$ (green) after the collapse.

cyclic analysis, without charge degradation, is also included. The charge efficiency was gradually decreased for up to 100 cycles, and this decrease was correlated with changes in the structural color (Fig. 4(a)). In detail, the change in structural color took the form of a change in the original peak of the reflectance spectra being separated into two small peaks of red and blue wavelengths after the charge degradation (Fig. 4(b)). Based on the optical characteristics, it is possible to infer a change in the nanostructure. The separation of two peaks means that the structure after the reaction does not have a two-dimensional periodicity, which is dissimilar to the original nanopore structure. This is an apt interpretation of the previous experimental observation of the longitudinally multipodal structure of $TiO_2$ *via* anodic growth as well.[38] The structure is numerically represented by a slit; therefore, we calculated fingerprinted reflectance spectra of the nano-slit structure (Fig. 4). The peak separation of calculated reflectance is in good agreement with the experimental spectra before and after nanostructure collapse (Fig. 4(b) and (d)). In the combined calculation of DFT and FDTD (Fig. 4(c) and S9 in ESI†), the distribution of the reflected amplitude of $\mathbf{E}_x$ in a slit was similar to the distribution of the values in hexagonal nanopores. On the other hand, the distribution of $\mathbf{E}_y$ is absolutely different from the values of a hexagonal porous structure, because the wave interference along the *y*-axis is in a planar direction along with the slit structure (Fig. 4(c) and Fig. S9 in ESI†). These results mean that the reflected amplitudes of $\mathbf{E}_x$ and $\mathbf{E}_y$ in the slit structure are rarely related, which causes a separation of the characteristic peak in the reflectance spectra of anatase and rutile $TiO_2$, as shown in Fig. S10 (ESI†).

## Conclusions

The structural colors and visible reflectance spectra of $TiO_2$ and $Li_xTiO_2$ are determined by the comprehensive effects of the refractive index and the wave interference that originates from crystalline development and from the nanostructure. With precise nanostructuring, the crystalline nature of a material could be obtained *via* analysis of the reflectance spectra. The phenomena whereby structural color represents crystalline and nanostructure qualities are described by *ab initio* principles and precisely interpreted by the reflectance spectra in various wavelengths. Previously, the real-time change in crystalline could only be detected using heavy equipment to accomplish X-ray adsorption near edge structure (XANES), extended X-ray adsorption fine structure (EXAFS) or Raman spectroscopy, none of which is often available for a routine operation. The proposed method in this study would allow material characterization using sophisticated cutting-edge tools that are simple and lightweight. Similar to XRD analysis, if the various reflectance spectra of nanomaterials are collected, it is possible to determine a crystalline change in unknown materials using the database. In addition, *in situ* analysis would be more easily conducted with the proposed method.

## Acknowledgements

This research was supported by the Global Frontier R&D Program of the Center for Multiscale Energy System funded by the National Research Foundation under the Ministry of Science, ICT & Future, Korea (NRF-2011-0031571).

## References

1 P. Vukusic and J. R. Sambles, *Nature*, 2003, **424**, 852–855.
2 A. R. Parker, *J. Opt. A: Pure Appl. Opt.*, 2000, **2**, R15–R28.

3 K. Kumar, H. Duan, R. S. Hegde, S. C. W. Koh, J. N. Wei and J. K. W. Yang, *Nat. Nanotechnol.*, 2012, **7**, 557–561.
4 A. C. Arsenault, D. P. Puzzo, I. Manners and G. A. Ozin, *Nat. Photonics*, 2007, **1**, 468–472.
5 K. Seo, M. Wober, P. Steinvurzel, E. Schonbrun, Y. Dan, T. Ellenbogen and K. B. Crozier, *Nano Lett.*, 2011, **11**, 1851–1856.
6 P. Hervé and L. K. J. Vandamme, *Infrared Phys. Technol.*, 1994, **35**, 609–615.
7 M. R. Lukatskaya, S.-M. Bak, X. Yu, X.-Q. Yang, M. W. Barsoum and Y. Gogotsi, *Adv. Energy Mater.*, 2015, **5**, 1500589.
8 K. Kang, Y. S. Meng, J. Bréger, C. P. Grey and G. Ceder, *Science*, 2006, **311**, 977–980.
9 Y. Li, K. Yan, H.-W. Lee, Z. Lu, N. Liu and Y. Cui, *Nat. Energy*, 2016, **1**, 15029.
10 G. Zheng, S. W. Lee, Z. Liang, H.-W. Lee, K. Yan, H. Yao, H. Wang, W. Li, S. Chu and Y. Cui, *Nat. Nanotechnol.*, 2014, **9**, 618–628.
11 A. G. Dylla, G. Henkelman and K. J. Stevenson, *Acc. Chem. Res.*, 2013, **46**, 1104–1112.
12 B. J. Morgan and G. W. Watson, *J. Phys. Chem. Lett.*, 2011, **2**, 1657–1661.
13 W. J. H. Borghols, M. Wagemaker, U. Lafont, E. M. Kelder and F. M. Mulder, *Chem. Mater.*, 2008, **20**, 2949–2955.
14 M. V. Koudriachova, S. W. Leeuw and N. M. Harrison, *Phys. Rev. B: Condens. Matter Mater. Phys.*, 2004, **69**, 054106.
15 H. N. Umh, S. Yu, Y. H. Kim, S. Y. Lee and J. Yi, *ACS Appl. Mater. Interfaces*, 2016, **8**, 15802–15808.
16 H. E. Prakasam, K. Shankar, M. Paulose, O. K. Varghese and C. A. Grimes, *J. Phys. Chem. C*, 2007, **111**, 7235–7241.
17 G. Kresse and J. Furthmüller, *Phys. Rev. B: Condens. Matter Mater. Phys.*, 1996, **54**, 11169–11186.
18 J. P. Perdew, K. Burke and M. Ernzerhof, *Phys. Rev. Lett.*, 1996, **77**, 3865–3868.
19 P. E. Blöchl, *Phys. Rev. B: Condens. Matter Mater. Phys.*, 1994, **50**, 17953–17979.
20 M. E. Arroyo-de Dompablo, A. Morales-García and M. Taravillo, *J. Chem. Phys.*, 2011, **135**, 054503.
21 B. J. Morgan and G. W. Watson, *J. Phys. Chem. C*, 2009, **113**, 7322–7328.
22 B. J. Morgan and G. W. Watson, *Surf. Sci.*, 2007, **601**, 5034–5041.
23 Y. S. Meng and M. E. Arroyo-de Dompablo, *Energy Environ. Sci.*, 2009, **2**, 589–609.
24 M. Gajdoš, K. Hummer, G. Kresse, J. Furthmüller and F. Bechstedt, *Phys. Rev. B: Condens. Matter Mater. Phys.*, 2006, **73**, 045112.
25 M. Fox, *Optical properties of solids*, Oxford university press, Oxford, 2001.
26 K. S. Yee, *IEEE Trans. Antennas Propag.*, 1966, **AP–14**, 302–307.
27 R. Su, R. Bechstein, L. Sø, R. T. Vang, M. Sillassen, B. Esbjörnsson, A. Palmqvist and F. Besenbacher, *J. Phys. Chem. C*, 2011, **115**, 24287–24292.
28 R. A. Spurr and H. Myers, *Anal. Chem.*, 1957, **29**, 760–762.
29 M. Hess, T. Sasaki, C. Villevieille and P. Novák, *Nat. Commun.*, 2015, **6**, 8169.
30 H. Kim, G. O. Park, Y. Kim, S. Muhammad, J. Yoo, M. Balasubramanian, Y.-H. Cho, M.-G. Kim, B. Lee, K. Kang, H. Kim, J. M. Kim and W.-S. Yoon, *Chem. Mater.*, 2014, **26**, 6361–6370.
31 K. Lasri, M. Dahbi, A. Liivat, D. Brandell, K. Edström and I. Saadoune, *J. Power Sources*, 2013, **229**, 265–271.
32 I. Nam, N. D. Kim, G.-P. Kim, J. Park and J. Yi, *J. Power Sources*, 2013, **244**, 56–62.
33 C. Dong, X. Li and J. Qi, *J. Phys. Chem. C*, 2011, **115**, 20307.
34 Q. Meng, Z. Guan, J. Huang, Q. Li and J. Yang, *Phys. Chem. Chem. Phys.*, 2014, **16**, 11519.
35 M. R. Palacín and A. de Guibert, *Science*, 2016, **351**, 1253292.
36 A. Barré, B. Deguilhem, S. Grolleau, M. Gérard, F. Suard and D. Riu, *J. Power Sources*, 2013, **241**, 680–689.
37 X. H. Liu, Y. Liu, A. Kushima, S. Zhang, T. Zhu, J. Li and J. Y. Huang, *Adv. Energy Mater.*, 2012, **2**, 722–741.
38 A. Mohammadpour, P. R. Waghmare, S. K. Mitra and K. Shankar, *ACS Nano*, 2010, **4**, 7421–7430.

 